



Topotactic phase transformations by concerted dual-ion migration of B-site cation and oxygen in multivalent cobaltite La–Sr–Co–O_x films

Jia Li^{a,b,1}, Meng-Xue Guan^{a,b,1}, Peng-Fei Nan^a, Jing Wang^{a,b,**}, Bing-Hui Ge^{c,****}, Kai-Ming Qiao^{a,b}, Hong-Rui Zhang^{a,b}, Wen-Hui Liang^{a,b}, Jia-Zheng Hao^a, Hou-Bo Zhou^{a,b}, Fei-Ran Shen^{a,b}, Fei-Xiang Liang^{a,b}, Cheng Zhang^{a,b}, Miao Liu^{a,b}, Sheng Meng^{a,b,d}, Tao Zhu^{a,d,f,*****}, Feng-Xia Hu^{a,b,d,*}, Tom Wu^e, Jian-Dong Guo^{a,b,d}, Ji-Rong Sun^{a,b,d}, Bao-Gen Shen^{a,b,d,g,***}

^a Beijing National Laboratory for Condensed Matter Physics, Institute of Physics, Chinese Academy of Sciences, Beijing, 100190, PR China

^b School of Physical Sciences, University of Chinese Academy of Sciences, Beijing, 100049, PR China

^c Institute of Physical Science and Information Technology, Anhui University, Hefei, Anhui, 230601, PR China

^d Songshan Lake Materials Laboratory, Dongguan, Guangdong, 523808, PR China

^e School of Materials Science and Engineering, University of New South Wales (UNSW), Sydney, NSW, 2052, Australia

^f Spallation Neutron Source Science Center, Dongguan, 523803, PR China

^g Institute of Rare Earths, Chinese Academy of Sciences, Jiangxi, 341000, PR China

ARTICLE INFO

Keywords:

Topotactic phase transformation
Perovskite cobalt oxides
B-site cation transfer
Brownmillerite structure
Electrocatalyst

ABSTRACT

Manipulating topotactic phase transformations *via* orderly ion transfer in complex oxides ABO_x is ubiquitous in advanced applications such as iontronics, ion-batteries and catalysts. Most of such ion-mediated transformations are accomplished by the transfer of oxygen or A-site ions. However, implementing the transformation *via* the transfer of B-site ions, despite the great challenge to overcome a large cohesive energy, has unique advantage since they host most functional properties of materials. Here, we present a tri-state phase transformation from perovskite (P) to brownmillerite (BM) and to single-layered perovskite (SL) structure *via* the concerted migration of oxygen and B-site Co-ions in La_{0.7}Sr_{0.3}CoO₃ thin films. Ac-STEM, XPS, XAS, PNR, magnetic and electric measurements demonstrated that presented B-site Co-cation transfer is along the CoO₄ tetrahedral sub-layer of the BM film, which leads to the reconfiguration of 3d-electrons and spin state in remanent Co ions and causes tremendous changes in magnetic and electric properties: from canted-antiferromagnetic insulator in BM phase to ferromagnetic insulator in SL phase. First-principles calculations revealed that the La³⁺-doping at A-site largely reduces the cohesive energy of Co-ions in CoO₄ and destabilize the CoO₄ tetrahedron of BM phase, which explains the formation of Co-ions transfer channel in the CoO₄ tetrahedral sub-layer. The present study highlights the effectiveness of regulating topotactic transformation *via* B-site ions transfer and provides a new pathway for manipulating the topotactic transformation with diverse functionalities.

* Corresponding author. Beijing National Laboratory for Condensed Matter Physics, Institute of Physics, Chinese Academy of Sciences, Beijing, 100190, PR China.

** Corresponding author. Beijing National Laboratory for Condensed Matter Physics, Institute of Physics, Chinese Academy of Sciences, Beijing, 100190, PR China.

*** Corresponding author. Beijing National Laboratory for Condensed Matter Physics, Institute of Physics, Chinese Academy of Sciences, Beijing, 100190, PR China.

**** Corresponding author. Institute of Physical Science and Information Technology, Anhui University, Hefei, Anhui, 230601, PR China.

***** Corresponding author. Beijing National Laboratory for Condensed Matter Physics, Institute of Physics, Chinese Academy of Sciences, Beijing, 100190, PR China.

E-mail addresses: wangjing@iphy.ac.cn (J. Wang), bhge@ahu.edu.cn (B.-H. Ge), tzu@iphy.ac.cn (T. Zhu), fxhu@iphy.ac.cn (F.-X. Hu), shenbg@iphy.ac.cn (B.-G. Shen).

¹ These two authors contributed equally to this work.

<https://doi.org/10.1016/j.nanoen.2020.105215>

Received 11 June 2020; Received in revised form 11 July 2020; Accepted 21 July 2020

Available online 14 August 2020

2211-2855/© 2020 Elsevier Ltd. All rights reserved.

1. Introduction

Transition-metal oxides (TMOs) exhibit a variety of intriguing phenomena resulting from the strong correlations between the transition metal valence electrons. Recently, ionic defects were found to play a key role in introducing or enhancing functionality in TMOs [1–9]. Of particular interest, the defects, including the oxygen vacancies and metal cations, can move out of and into the sample at specific temperatures and electric fields, causing exotic phenomena such as magnetic ordering, metal-insulator transition, ferroelectric polarization and even structural transitions [10–14]. Moreover, ion migration and related phenomena can be controlled by electric fields due to the charged nature of ions, which renders TMOs broad application prospects in information, catalysis and energy storage [4,15–17]. Actually, a lot of studies have demonstrated that binary oxides or ternary TMOs (or complex oxides) with ABO_x ($2 \leq x \leq 3$) structure can be harnessed for chemical sensors, membrane, iontronics, solid oxide fuel cell (SOFC), ion batteries and catalysts by controlling ion transfer [2,4,15–24].

Many efforts have been devoted to exploiting effective methods to implement orderly ion migration in these materials, and thus to modulate their various novel properties [12,25–29]. It has been reported that thin films of perovskite (P) cobalt and iron oxides (ABO_3) can be converted into the brownmillerite (BM) structure ($ABO_{2.5}$) through a topotactic phase transformation by regulating the orderly loss of oxygen ions [12,29–31]. Recently, investigations further demonstrated that ionic liquid gating can produce reversible topotactic phase transformation between perovskite $SrCoO_3$ film and BM $SrCoO_{2.5}$ film by driving the flow of oxygen ions, and even can insert protons into the tetrahedral layer of BM $SrCoO_{2.5}$ to prepare a weakly ferromagnetic insulator $HSrCoO_{2.5}$ [ref.10]. All these studies conceivably show that the topotactic phase transformation and thus corresponding changes in magnetic, optical and electric properties can now be achieved by elaborately controlling the migration of either light A-site cation or oxygen ions [32–36].

Meanwhile, many studies have demonstrated that the oxygen content controlled by topotactic transformation in complex oxides plays a key role in applications of oxygen electrocatalysis for energy storage and conversion technologies, which represents a promising strategy to improve the performance of SOFC cathodes via utilizing the topotactic transformation in multivalent transition metal oxides [12]. Moreover, the topotactic progress in ABO_x usually leads to the reversible variation in the e_g occupancy of B-site, which has been regarded as an important activity descriptor of oxygen reduction reaction (ORR) and oxygen evolution reaction (OER) [37–39]. This unique character of modulating e_g occupancy in topotactically transformed materials is particularly useful in developing bifunctional catalysts for devices capable of both storing and converting energy.

On the other hand, it has been demonstrated that spin state of B-site ions directly influences electronic conductivity and catalytic activity towards oxygen reduction and evolution [37,40,41]. Actually, as the carrier of strongly-correlated d -electrons, B-site cations (usually transition-metal ions) host most functional properties of ABO_x , such as charge/orbital/spin ordering, Mott transition, catalysis and nonlinear optic. While the A-site cations with large radii are mainly responsible for the structure stabilization and modify the valence of B-ions. Obviously, manipulating the topotactic phase transformation *via* directly controlling the B-site ions transfer can largely enrich materials' functionalities and provide a special opportunity to discover new phenomena concerning the topotactic transformation. Specially, controlling varied magnetic and electrical properties in topotactically transformed materials *via* B-site ions transfer therefore probably could be used to monitor the dynamic change in oxygen reduction and/or evolution activities for energy generation and storage devices. However, there are few studies focusing on regulating the phase transformation *via* driving the migration of B-site ions, partially due to the relatively high cohesive energy needed for the migration of B-site ions.

Cobaltite oxides have been regarded as ideal platforms for studying topotactic phase transformation [10,12] due to the rich multivalent characteristics of Co ions. However, it is very hard to realize multistep topotactic transformation in $SrCoO_x$ due to the relative high thermodynamic stability of $SrCoO_{2.5}$. Here, we report a tri-state topotactic phase transformation induced by concerted dual ions transfer of B-site ions and oxygen in the La^{3+} -doped $La_{0.7}Sr_{0.3}CoO_3$ thin film. By taking advantages of the different stability of multivalent Co ions in cobaltites [42,43], we achieved the concerted transfer of B-site cobalt ions and oxygen under a two-step vacuum annealing, leading to the successive transformation from perovskite (P) to brownmillerite (BM) and then to single-layered perovskite (SL) structure (Fig. 1a). Associated with such concerted migration of dual ions, a specific rearrangement of $3d$ orbital occupation and spin state for Co ions occurs, resulting in stark changes in magnetic and electric properties. Aberration-corrected scanning transmission electron microscopy (ac-STEM), X-ray photoelectron spectroscopy (XPS), and absorption spectroscopy (XAS) demonstrated that presented B-site Co-cation transfer is along the CoO_4 tetrahedral sub-layer of the BM $La_{0.7}Sr_{0.3}CoO_{2.5}$ film. First-principles calculations and related analysis revealed that the La^{3+} -doping at A-site largely reduces the cohesive energy of Co-ions and thus the stability of Co–O bond in CoO_4 tetrahedron of BM structure, which explains the formation of the unique transfer channel for Co-ions in the CoO_4 tetrahedral sub-layer. Our findings demonstrate a distinct migration mechanism of B-site ions in ABO_x complex oxides, providing a new way for manipulating the topotactic transformation with diverse functionalities.

2. Experimental and theoretical methods

2.1. Growth of perovskite $La_{0.7}Sr_{0.3}CoO_3$ films and thermal annealing process

Epitaxial $La_{0.7}Sr_{0.3}CoO_3$ (113-LSCO) films were deposited on (001) $(LaAlO_3)_{0.3}(SrAl_{0.5}Ta_{0.5}O_3)_{0.7}$ (LSAT) substrate by pulsed laser deposition technique. Deposition temperature is 700 °C and the O_2 pressure is 25 Pa. The laser (KrF, $\lambda = 248$ nm) energy density used is 1.2 J/cm² and the frequency is 2 Hz. After the deposition, samples were slowly cooled down to room temperature at a rate of 8 °C per minute under an O_2 pressure of 100 Pa. The thickness of the film was controlled by growth time, and further checked by the X-ray reflectometry. All the samples except the $La_{0.7}Sr_{0.3}CoO_{2.5}$ (1125-LSCO) film used in magnetic and polarized neutron reflectometry (PNR) measurements have thickness of ~33 nm. While for the PNR and corresponding macroscopic magnetic measurements, a slightly thicker 1125-LSCO film (~50 nm) was chosen so as to catch the effective signals during the PNR collections. To induce the multistep topotactic phase transformation, the original as-grown 113-LSCO films were heated at 300 °C and 450 °C, respectively, for 15 min at a vacuum of 10^{-6} Pa (see supplementary Fig. S1 and Note S1 for more information about the annealing experiments). Subsequently, the sample was naturally cooled down to room temperature under the same vacuum. Moreover, to examine the reversibility of the topotactic transformation, the reversed oxygen annealing experiments was carried out on the fresh SL $La_{1.4}Sr_{0.6}CoO_4$ film at 800 °C under flowing oxygen with a flux of 40 ml/min for 2hr, accompanied with a natural cooling process to room temperature under the same oxygen atmosphere. The crystalline structures for all films were checked by X-ray diffraction (XRD), and reciprocal space mapping (RSM) using high-resolution four-circle diffractometer (Smartlab, Rigaku).

2.2. HAADF-STEM, ABF-STEM, EDS and EELS measurements

The cross-sectional specimens investigated by ac-STEM were prepared by a focus ion beam system (FEI Helios 600i). High-angle annular dark field STEM (HAADF-STEM) imaging, annular bright field STEM (ABF-STEM) imaging, energy dispersive X-ray spectrum (EDS) and electron energy-loss spectroscopy (EELS) measurements were carried

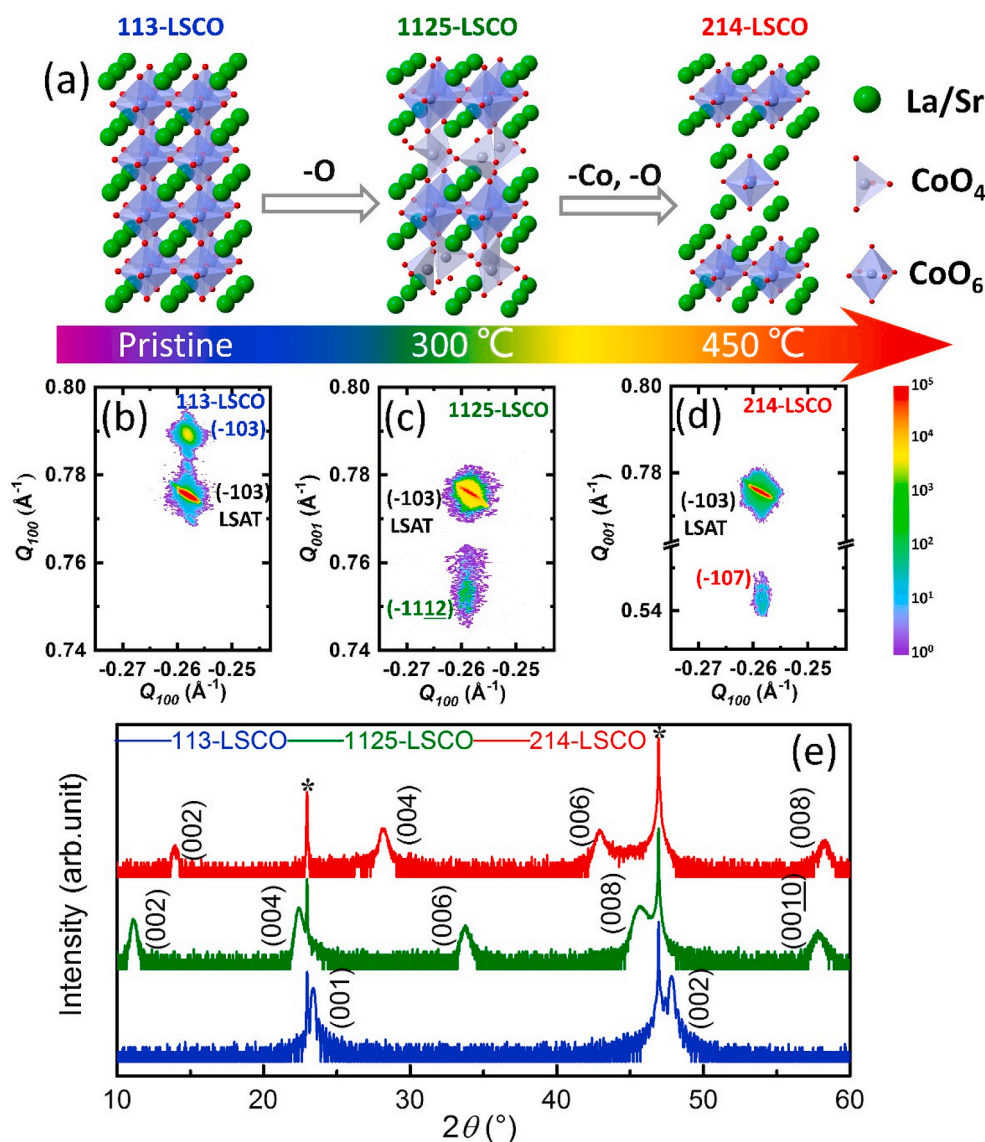


Fig. 1. Topotactic structural transformations among $\text{La}_{0.7}\text{Sr}_{0.3}\text{CoO}_3$ (113-LSCO), $\text{La}_{0.7}\text{Sr}_{0.3}\text{CoO}_{2.5}$ (1125-LSCO) and $\text{La}_{1.4}\text{Sr}_{0.6}\text{CoO}_4$ (214-LSCO). (a) Crystal model diagrams of 113-LSCO, 1125-LSCO and 214-LSCO phases. RSMs of (b) 113-LSCO, (c) 1125-LSCO and (d) 214-LSCO films. (e) XRD θ - 2θ scans of the 113-LSCO (blue), 1125-LSCO (green) and 214-LSCO (red) films on (001)-LSAT substrates. Numbers in parentheses correspond to crystallographic planes of the peak.

out using a JEOL ARM 200F microscope, equipped with double spherical aberration correctors and GIF quantum 965.

2.3. XAS, XPS measurements

The XAS data was obtained at Beamline BL08U1A of Shanghai Synchrotron Radiation Facility. The XPS results were measured by X-ray Photoelectron Spectrometer (Thermo Fisher Scientific ESCALAB 250X) produced by Thermo Fisher Scientific. The X-ray source is a monochromatic Al $K\alpha$ ray ($h\nu = 1486.6$ eV). Both XAS and XPS measurements were carried out at room temperature.

2.4. Magnetic and electrical transport characterization

The magnetic and electrical transport properties of the samples were characterized by a superconducting quantum interference device vibrating sample magnetometer (SQUID-VSM), equipped with an electric-measurement module. We used a sourcemeter (Keithley 2601) and a nanovoltmeter (Keithley 2182) to measure electrical transport properties of perovskite $\text{La}_{0.7}\text{Sr}_{0.3}\text{CoO}_3$ film with a four-point method,

and a source measure unit (Keithley 2611) to measure that of BM $\text{La}_{0.7}\text{Sr}_{0.3}\text{CoO}_{2.5}$ and SL $\text{La}_{1.4}\text{Sr}_{0.6}\text{CoO}_4$ films with a two-point method.

2.5. Polarized neutron reflectometry measurements

Polarized neutron reflectometry (PNR) measurements were carried out at the instrument multi-purpose reflectometer (MR) at China Spallation Neutron Source (CSNS) to detect the magnetic information of 1125-LSCO film. The experiments were performed under 0.9T magnetic field at 10 K. MR is a time-of-flight instrument with a neutron wavelength (λ) band from 2 to 7 Å and resolution $\Delta\lambda/\lambda$ of 10%. Neutron beam impinges onto the sample with an incident angle θ_i ($\theta_1 = 0.3^\circ$, $\theta_2 = 0.5^\circ$, and $\theta_3 = 1.0^\circ$) and collected by a ^3He detector. The collected data was fitted using the *Genx* software package [44].

2.6. First-principles calculations

The DFT calculations were performed with the Vienna *ab initio* simulation package (VASP). Generalized gradient approximation in the PBE form was used to account for electron exchange and correlation

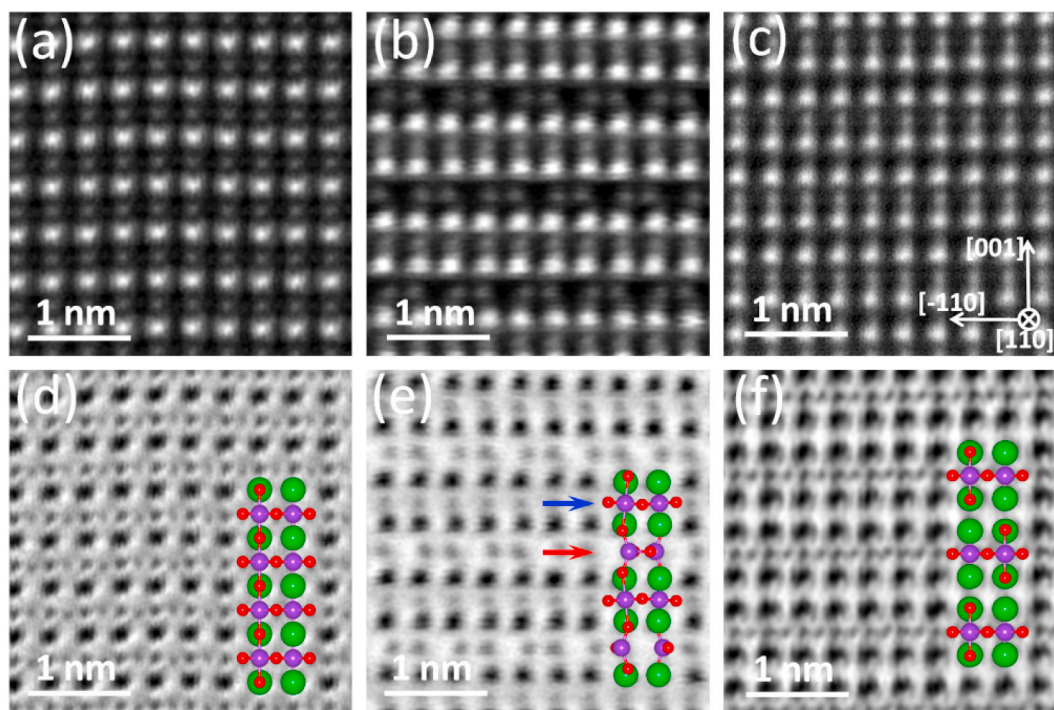


Fig. 2. Structural analysis of 113-LSCO, 1125-LSCO and 214-LSCO films. Cross-sectional Z-contrast HAADF-STEM images of (a) 113-LSCO film, (b) 1125-LSCO film and (c) 214-LSCO film. ABF images of (d) 113-LSCO film, (e) 1125-LSCO film and (f) 214-LSCO film. Atoms at La/Sr-, Co- and O- sites are indicated by green, violet and red spheres, respectively. In Fig. 2e, the tetrahedral and octahedral layers are marked by red and blue arrows, respectively.

effects. To satisfy the total-energy convergence of less than 0.001 eV/atom, typical computational parameters for calculations include a plane-wave energy cut-off of 500 eV, a $10 \times 10 \times 6$ Monkhorst–Pack k -point sampling mesh with respect to the perovskite unit cell (containing 36 atoms here), and a $0.01 \text{ eV}\text{\AA}^{-1}$ force tolerance on each atom for structural relaxation. We have included the strong correlation effects of cobalt d electrons by means of the GGA + U scheme, with the on-site Coulomb interactions of $U = 4.5 \text{ eV}$ and on-site exchange interactions of $J = 0.5 \text{ eV}$. All calculations involving magnetism employ an initial G-type antiferromagnetic state and correct the exchange correlation function with the Vosko–Wilk–Nusair interpolation, while all magnetic moments were allowed to freely relax.

3. Results and discussion

3.1. Topotactic structural transformations

We performed experiments using epitaxial and high-quality perovskite 113-LSCO thin films which were deposited on (001)-LSAT substrates by pulsed laser deposition. Vacuum annealing experiments under elevated temperatures of 300 °C and 450 °C were performed on the as-grown films, resulting in distinct structural transitions between different phases, as shown in Fig. 1. Fig. 1e shows the comparison of XRD patterns for as-grown, 300 °C and 450 °C annealed samples, which will be hereafter termed as samples B and S, respectively.

The characteristic peaks of typical perovskite structure (at around 23.4° and 47.8°) were observed for the as-grown sample (blue trace in Fig. 1e), consistent with previous reports [45,46]. The emergence of (002), (006) and (010) super-structural peaks at about 11.1°, 33.8° and 57.9°, together with the disappearance of perovskite characteristic peaks, indicates the formation of alternately stacking of CoO_6 octahedron and CoO_4 tetrahedron *i.e.* a long-range ordered BM structure in sample B (green trace) [10,12,47]. Thus, the phase in sample B should be BM $\text{La}_{0.7}\text{Sr}_{0.3}\text{CoO}_{2.5}$ (1125-LSCO). This long-range BM structure is commonly observed in the $\text{SrCoO}_{2.5}$ film, but rarely reported in

La^{3+} -doped $\text{La}_{1-x}\text{Sr}_x\text{CoO}_{2.5}$ ($0 \leq x < 1$) film. While for sample S, the characteristic peaks of BM structure completely disappear, and a new diffraction peak appears at about 42.9° (red trace), suggesting the emergence of a new phase in sample S. Note that diffraction patterns of sample S are totally different from that of 1125-LSCO and 113-LSCO, indicating a dramatic structural transformation during the annealing at 450 °C. Comparing the diffraction patterns of sample S to the diffraction database demonstrates that our results are consistent with that of the K_2NiF_4 type Ruddlesden-Popper phase (A_2BO_4), *i.e.* the single-layered perovskite [48]. Meanwhile, the diffraction peaks of sample S at 28.2°, 42.9° and 58.3°, corresponding to (004), (006) and (008) diffraction peaks, respectively, also agree well with previous reported results [49] on $\text{La}_{2-x}\text{Sr}_x\text{CoO}_4$ with SL structure.

Fig. 1b,c,d show the XRD RSMs of all three samples around the LSAT substrate's (-103) Bragg reflections. It was found that the corresponding reflections of all films were aligned with their substrates along the Q_{001} direction. This result indicates that the in-plane lattice constant of each film regardless of structure is coherently maintained as the substrate, manifesting the characteristics of topotactic structural transformations. Moreover, XRD measurements for the sample annealed under 400 °C show that no intermediate structure emerges in the evolution from 1125-LSCO to 214-LSCO (see Supplementary Fig.S2), demonstrating that the topotactic transformation from BM to SL structure driven by thermal power is straightforward without the formation of intermediate phase.

To reveal the micro-structural variation at atomic scale during the transformation, the ac-STEM experiments were carried out on all three samples. Fig. 2 illustrates both HAADF- and ABF-STEM images for all films. Firstly, one can find that the B-site Co ions exhibit obvious coordinate changes in three samples: from a periodic octahedral geometry (as-grown sample) to an alternately stacking of octahedron and tetrahedron along [-110] direction (sample B), and then to a staggered arrangement of octahedral geometry with one-layer intervals along [001] direction (sample S). The atomic alignments recognized from both HAADF and ABF images (Fig. 2a–f and Supplementary Fig. S3) of three

samples agree well with the theoretical crystal structure of P, BM and SL, respectively (the inset of Fig. 2d–f).

Specially, the distribution of oxygen ions in the crystal lattice of sample S was deduced from ABF images (see Supplementary Fig. S4a and Fig. S4c). From the image acquired along [010] direction, four oxygen atoms around the nearest neighbor of a cobalt atom were affirmed (supplementary Fig. S4b). While in the image acquired along [110], two nearest neighbor oxygen atoms were recognized (Supplementary Fig. S4d). Such different oxygen coordination numbers around the Co atoms obtained along different directions manifest the existence of CoO₆ octahedral sub-layer in the sample S. Meanwhile, by comparing the atomic arrangement in the HAADF images acquired along [010] and [110] directions, one can find that the CoO₆ sub-layer staggers with each other by a shift of half an unit cell along in-plane [110] direction (See Fig. 1a, Supplementary Fig. S3c and Fig. S3d), forming the SL structure. Moreover, based on these results together with the fact that no obvious segregation of La/Sr was found in EDS measurements on sample S (see supplementary Fig. S5), one can identify the chemical formula of the new phase in sample S as La_{1.4}Sr_{0.6}CoO₄, i.e. 214-LSCO.

Furthermore, the variation of atomic occupation during the transformation, which contains the information of ions transfer and rearrangement, were checked by the comparison of vertical La/Sr–La/Sr interplane distances for all three phases. The data were extracted from respective HAADF images, and illustrated in Fig. 3 (see also supplementary Fig. S3). Firstly, one can find that the periodic modulation of sub-layer parameters (blue, green, and red symbols) is consistent with that calculated from the XRD results (dashed lines) for all three films. A single La/Sr–La/Sr interplane distance of ~3.9 Å (blue symbols) was identified for the 113-LSCO film, which agrees well with the periodic alignment of CoO₆ layer. Meanwhile, the observed alternately varying La/Sr–La/Sr interplane distances (between ~4.5 Å and ~3.5 Å) in 1125-LSCO phase (green symbols) correspond to the emergence of an oxygen-deficient CoO₄ tetrahedral sub-layer in between two CoO₆ octahedral sub-layers due to the orderly extraction of oxygen ions, indicating the formation of BM structure. More interestingly, in comparison with 1125-LSCO phase, the La/Sr–La/Sr interplane distance of 214-LSCO phase keeps nearly unchanged in the octahedral sub-layers (~3.5 Å), but decreases from ~4.5 Å to ~2.9 Å (see red symbols in Fig. 3) in the tetrahedral sub-layers accompanied with the vanishing of CoO₄ tetrahedrons. These results strongly suggest that the concerted transfer of oxygen and B-site Co ions in the tetrahedral sub-layers, facilitated by thermal power, should be the dominant mechanism behind the continuous structural transformation from P to BM and then to SL structure.

3.2. Evolution of chemical states and Co-clusters

Such new progress of concerted transfer of oxygen and B-site Co ions would bring about big changes in electronic configuration and thus the

valence state of Co-ions. Moreover, the one-half reduction of Co content in the chemical composition of 214-LSCO phase in comparison with that of 1125-LSCO suggests that an orderly migration of Co ions from the frame structure of 1125-LSCO occurs during the topotactic transformation from BM to SL phase. More experiments are required to demonstrate the fate of these transferred Co atoms besides the chemical state variation of Co-ions in the film, which is important for well understanding the new topotactic transformation driven by B-site ion-transfer. For this purpose, spectrum measurements using multiple means of XAS, XPS and EELS, whose detecting areas range from local atomic scale to several hundred micrometer-scale (XAS~50 nm, XPS~200–900 μm and EELS~0.2 nm), were performed on all three films, as shown in Fig. 4, so that the variation of Co valence state and chemical environment during the tri-state topotactic transformation could be crosschecked by comparing local microscopic results and macroscopic average ones.

Firstly, XAS measurements on three films show that XAS peak positions of cobalt *L*-edge (Fig. 4a) shift to lower energy for the La–Sr–Co–O_x film from 113- to 1125- and to 214-LSCO, which indicates a continuous decrease of average valence states of cobalt [10,29,50] during the topotactic transformations from perovskite 113-LSCO to BM 1125-LSCO and to SL 214-LSCO. Specially, a chemical shift of more than 1 eV towards low energy was recognized from 1125-LSCO to 214-LSCO film. In addition, the oxygen *K*-edge results (Fig. 4b) show a continuous decrease in the feature relating with the hybridization between the 3*d*-/4*s*-orbital of cobalt and 2*p*-orbital of oxygen (see pre-edge peak A and peak D in Fig. 4b) when 113-LSCO transforms to 1125-LSCO and to 214-LSCO film [10,12,29,50–52]. Meanwhile, the intensification of peak B, which is related to the square-pyramidal coordination of Co-ions during the topotactic reduction, generally indicates an increase in oxygen vacancies [52–54], which can be clearly identified for 214-LSCO (Fig. 4b). While the non-distinct change of peak B after the P-BM transformation is probably attributed to the oxygen absorption and resultant change of square-pyramidal coordination, which suppresses the visibility of peak B in 1125-LSCO film. Note that the present 1125-LSCO film with La³⁺ doping behaves unstable, which can even absorb oxygen and transform towards the ABO₃ perovskite structure when it is placed in air at room temperature for a long time (see supplementary Fig. S10). The suppression of cobalt-oxygen hybridization and increase of the oxygen vacancy confirm the decrease of the average valence state of cobalt in La–Sr–Co–O_x films during the successive tri-state topotactic transformations from 113-LSCO to 1125-LSCO and to 214-LSCO.

However, a quantitative analysis by EELS, which definitely focused on the 1125-LSCO and 214-LSCO structure, provides values of +2.38 and +2.46 for Co valence in 1125-LSCO and 214-LSCO phase, respectively (see Supplementary Fig. S6 and Supplementary Note S2). Such increasing trend of Co valence state from 1125-LSCO to 214-LSCO phase appears to be inconsistent with the XAS results, where the obtained

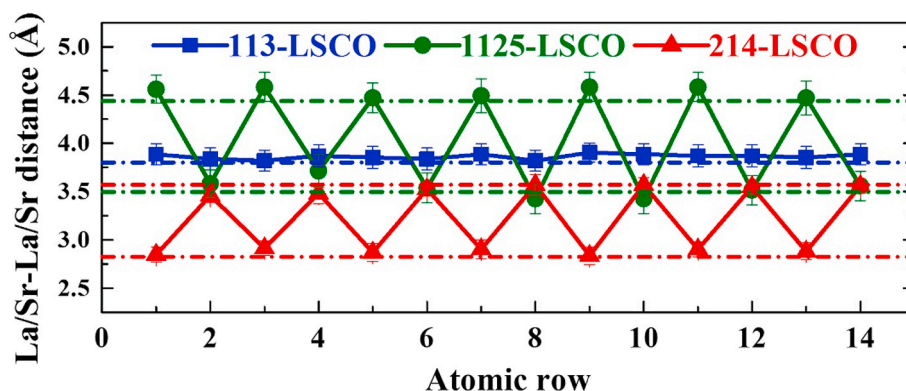


Fig. 3. Comparison of statistical analysis of HAADF-STEM results (solid symbols) with XRD results (dashed lines) for out-of-plane La/Sr–La/Sr atomic layer distances of 113-LSCO (blue), 1125-LSCO (green) and 214-LSCO phases (red), respectively.

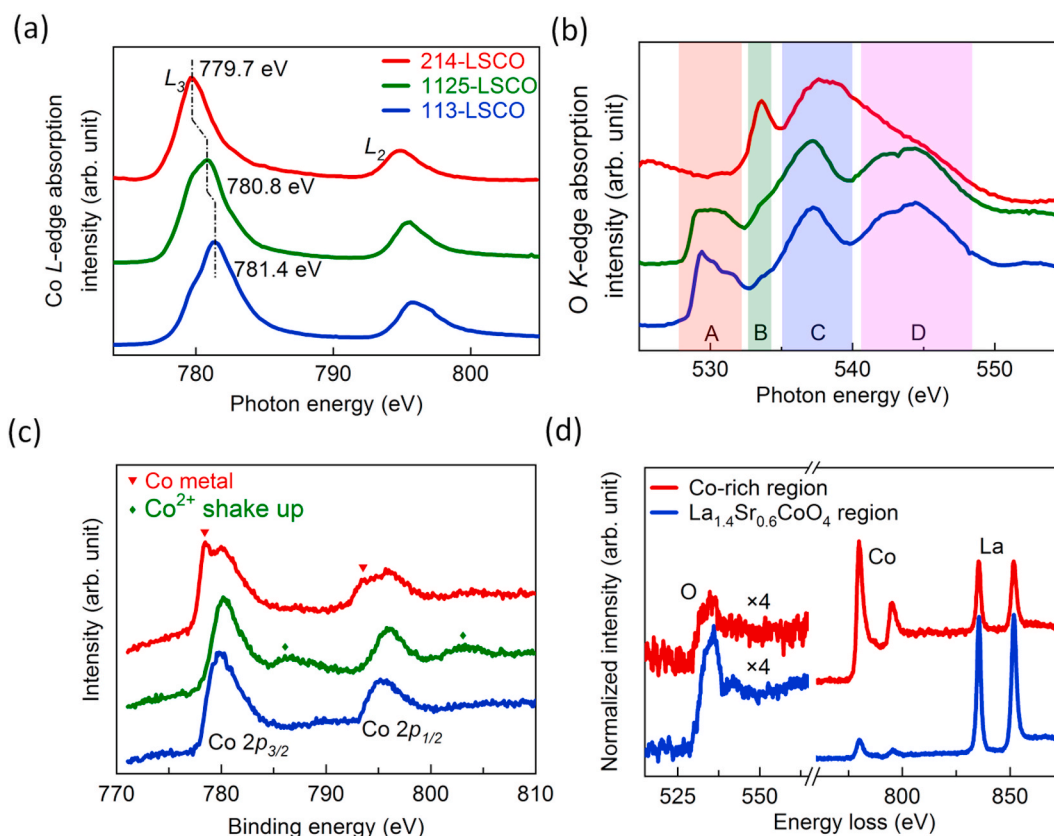


Fig. 4. Co-ions valence evolution among 113-LSCO, 1125-LSCO and 214-LSCO films. XAS of (a) Co *L*-edge and (b) O *K*-edge for three films. O *K*-edge XAS results were normalized with respect to the intensity of peak C, which represents La/Sr–O hybridization. (c) XPS spectra for Co 2*p* in three films. (d) Comparison of O *K*-edge, Co *L*-edge and La *M*-edge EELS spectra between the 214-crystalline region and Co-rich region in the 214-LSCO film.

average Co valence state of the 214-film (including 214-phase and Co-clusters, discussed thereafter) exhibits a monotonous reduction comparing with that of 1125-LSCO film, but agrees with the theoretical values calculated from the chemical formula (+2.30 for 1125-LSCO phase and +2.60 for 214-LSCO phase).

It is worth noting that the detecting area of XAS (~ 50 nm) is much larger than that of EELS (~ 0.2 nm), while the EELS measurements were definitely focusing on 214-LSCO structure (determined from STEM observations). Thus, the opposite evolution trend of Co valence state for XAS and EELS measurements implies that lower valence or elementary Co atoms may exist in the 214-film. Considering that the B-site cobalt ions migrated out from the frame structure of BM 1125-LSCO cannot release to ambient atmosphere, one can conclude that the reduction of average Co valence for 214-LSCO film indicated by XAS measurements should originate from the contribution of the migrated Co locating in the 214-LSCO film, which pulls down the average cobalt valence of the whole film.

Fig. 4c shows XPS results for three films, from which a large amount of Co^{3+} ions can be identified from the Co-2*p* spectrum in the 113-LSCO film [55–57]. Moreover, compared to 113-LSCO film, two extra satellite peaks appear beside the Co $2p_{3/2}$ and Co $2p_{1/2}$ main peaks in the spectrum of 1125-LSCO film, which indicates the emergence of Co^{2+} ions [40,56–60] during the perovskite 113-LSCO to BM 1125-LSCO transformation. More importantly, in the 214-LSCO film, such satellite peaks almost vanish. Instead, two strong Co-metal peaks appear at 778.6 eV and 793.6 eV, respectively, which correspond elementary Co. This result strongly suggests that the Co atoms migrated out from the structure framework of 1125-LSCO may assemble together and form Co-rich areas, that is composed mainly by elementary Co, in the 214-LSCO matrix [57,58].

Ac-STEM observations indeed demonstrated that some clusters are

embedded in the 214-LSCO matrix randomly. Fig. 5 displays the typical HAADF-STEM image of a cluster and around. Note that a fuzzy layer of 214-SL structure still covers the cluster. EELS measurements were also performed on the cluster regions, which shows that the intensity ratio of

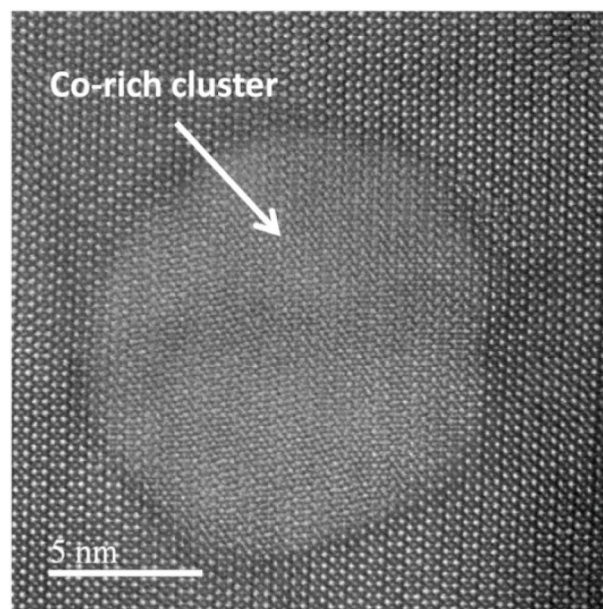


Fig. 5. HAADF-STEM measurements of a cobalt-rich cluster embedded in the 214-LSCO film. The circular area indicated by the white arrow with different contrasts is the cobalt-rich cluster.

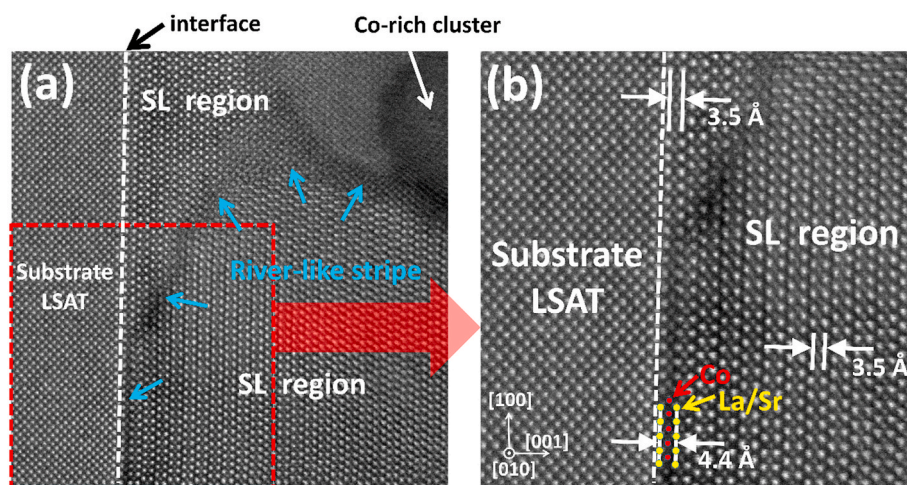


Fig. 6. (a) Typical river-like channel of Co-ions transfer observed in the HAADF-STEM image of 214-LSCO film. Substrate LSAT, Co-rich cluster and SL-crystalline regions are marked in the image, respectively. The river-like dark stripe is indicated by light blue arrows. (b) The enlarged view of the red boxed area in Fig. 6a. The zone axis in images are along the [010] direction of LSAT.

Co/La in the cluster region (~ 2.0 , see the right part of Fig. 4d) is much higher than that in 214-LSCO crystalline region (~ 0.14). Meanwhile, the EELS O K -edge intensity in such cluster region is almost a quarter of that in 214-crystalline region (the left part of Fig. 4d). These results strongly demonstrate the Co-rich nature of the clusters. Furthermore, EDS standardless quantitative analysis on the Co-rich region (see Supplementary Fig. S5 and Supplementary Table S1) demonstrates that the Co atomic percentage is as high as 68.4%, much higher than that of La (12.8%), Sr (2.3%) and O (16.5%), which is in line with the EELS results, unambiguously demonstrating the Co-rich nature of the observed clusters by ac-STEM.

3.3. Experimental evidence of Co-migration channel and first-principles calculations

The structural analysis of La–Sr–Co–O_x films in section 3.1 above has indicated that the topotactic transformation from BM and SL phase is induced by the concerted migration of oxygen and B-site Co ions along the CoO₄ tetrahedral sub-layer. To search for hints of possible migration channel of Co-ions, we carefully investigated the structure of the micro-area around the Co-clusters by ac-STEM.

Fig. 6 presents a typical STEM-HAADF image of the area around a Co-rich cluster. One can find a river-like stripe with anomalous dark contrast in the image, connecting the Co-rich cluster. From the end of this strip that connects the Co-rich cluster, a distorted structure extending to the middle of this stripe can be identified (Fig. 6a). While at another end of the strip away from the cluster, an orderly alignment of Co atom in between two La/Sr-arrays is recognized (see the red dots, the lower middle part of the image in Fig. 6b), which indicates an orderly Co–O sub-layer. Furthermore, the La/Sr–La/Sr interplane distance (the yellow lines of Fig. 6b) of this sub-layer was carefully measured from the image and determined to be 4.4 Å. This value is much larger than that of the CoO₆ octahedral layer (3.5 Å) in 214-LSCO phase (the distance between white lines in Fig. 6b, also see the diagram in Fig. 1a and La/Sr–La/Sr distance in Fig. 3), but agrees well with the La/Sr–La/Sr distance of CoO₄ tetrahedral sub-layer (4.5 Å) in 1125-LSCO structure (see Figs. 1a and 3). To rule out possible effect by substrate, we further checked the layer outside the stripe but at similar position adjacent to the interface (see the upper part of Fig. 6b), and obtained a normal La/Sr–La/Sr interplane distance of CoO₆ octahedral layer (3.5 Å) in 214-LSCO phase, which suggests that the possible effect from the substrate is not the reason for the observed large La/Sr–La/Sr interplane distance in the stripe. These results largely indicate that the observed orderly Co–O layer in the stripe is a residual CoO₄ sub-layer of 1125-LSCO phase

during the topotactic transformation from BM to SL.

The river-like stripes observed in the STEM image, which connects the Co-rich cluster and the residual CoO₄ sub-layer in the SL 214-LSCO phase, exhibit the trace of Co ions migration channel and record the evolution of the collapse “disaster” of CoO₄ tetrahedral sub-layer caused by the migration of Co ions. This result evidences that the migration channel of Co-ions during the topotactic transformation from 1125-LSCO to 214-LSCO phases is along the CoO₄ tetrahedral sub-layer. Moreover, the observation of residual migration channel further confirms that the Co-rich clusters embedded in 214-LSCO film are formed by those Co atoms migrated out from CoO₄ tetrahedrons in 1125-LSCO phase.

Furthermore, to reveal the underlying mechanism for the formation of Co-ion migration channel in the CoO₄ sub-layer, we carried out first-principles calculations on the BM La_{0.625}Sr_{0.375}CoO_{2.5} and calculated the cohesive energy for different site atoms in the structure, which provides a quantitative characterization of the ease of atom flowing out from the BM structural frame. The cohesive energy, E_c , is defined as the energy that must be supplied to the solid to separate its constituents into neutral free atoms at rest and at infinite separation with the same electronic configuration [61,62]:

$$E_c = (E_{defect} + NE_i - E_{tot})/N, \quad (1)$$

where E_{tot} is the total energy of primitive BM structure, E_{defect} is the energy of BM structure with a B-site or an oxygen vacancy, E_i is the energy per Co/La(Sr) atom in the elemental solid or O atom in the oxygen molecule, and N is the number of vacancy. The calculated results (see Supplementary Fig. S8b and Supplementary Note S3) show that the cobalt vacancy in the CoO₄ tetrahedral sub-layer has a lower E_c (0.58 eV per La_{0.625}Sr_{0.375}CoO_{2.5} unit cell) in comparison with oxygen atoms (0.61 eV per La_{0.625}Sr_{0.375}CoO_{2.5} unit cell) in the CoO₆ octahedral sub-layer. These results demonstrate that the CoO₄ tetrahedron in 1125-LSCO is more unstable than CoO₆ octahedron. As a result, the Co–O bonds in the CoO₄ tetrahedral sub-layer of BM 1125-LSCO tend to break down firstly with an extra energy provided and release the cobalt atoms from CoO₄ sub-layer, leading to a distinct B-site cobalt ions migration.

In previous studies, annealing or bias voltage were used to drive ions to escape or inject into materials [10,11,25,63]. However, these studies mainly focused on the regulation of either oxygen ions or A-site metal cations in ABO_x materials. In our experiments, the oxygen ions initially overcome the vacancy activation energy barrier and flow, due to its good mobility, under the condition of high vacuum and 300 °C. In this process, some Co–O bonds break up and O atoms diffuse to the

surface of the film, combining to form O_2 and detaching from the film [12,64]. Such orderly loss of O atoms from the structural framework leads to the transformation from P to BM phase with alternately stacked CoO_6 octahedral and CoO_4 tetrahedral sub-layers (Fig. 2b, e) [12, 64–66]. Note that the appearance of CoO_4 tetrahedral sub-layers is equivalent to opening Co-ion migration channels for the film, which has been demonstrated as an oxygen transfer channel in materials of $CaFeO_{2.5}$ [47]. As the vacuum annealing temperature keeps rising to 450 °C, the kinetic energy of the atoms in the crystal lattice further increases, leading to the breakdown of the CoO_4 tetrahedrons in the BM structure and the outflow of cobalt atoms (together with or after the oxygen atoms) from the lattice frame. As a result, the evacuated tetrahedral sub-layer collapses and the octahedral sub-layers rearrange, eventually forming the 214-SL structure.

3.4. Variation of magnetic and transport behaviors

Owing to the transfer of oxygen and B-site Co ions, the occupation of d-orbital and the spin state of Co-ions can change markedly. As a result, tremendous changes in physical properties should occur accompanying with the tri-state topotactic phase transformation. Fig. 7 shows the measured magnetic and electrical transport properties for 113-LSCO, 1125-LSCO and 214-LSCO films. Firstly, a good ferromagnetic metal state at low temperatures with a saturated magnetization about $\sim 1.37 \mu_B/Co$ (10 K) was observed in the perovskite 113-LSCO film (Fig. 7b,d). The determined Curie temperature (about 197 K) is slightly lower than that of the bulk material, which is probably caused by the in-plane epitaxial tensile strain [41,67].

As the sample transforms from perovskite to BM structure owing to the flow of oxygen ions, a weak ferromagnetism with a small net saturation magnetization about $\sim 0.53 \mu_B/Co$ (10 K) was deduced from the measured M-H curve for 1125-LSCO (Fig. 7b,d). Meanwhile, the electrical transport changes from metallic to insulating behavior. The large decrease in the saturated magnetization implies the change of spin structure. Considering that the crystal structure of present 1125-LSCO is similar to that of $SrCoO_{2.5}$, one may speculate that a similar magnetic ground state also appears in 1125-LSCO. However, previous studies have demonstrated that $SrCoO_{2.5}$ behaves a G-type antiferromagnetic state [10,12,68], where a complete compensation occurs both within the CoO_6 octahedral and CoO_4 tetrahedral layers and between them. The observed non-zero magnetization in our 1125-LSCO with La^{3+} doping seems inconsistent with the results of $SrCoO_{2.5}$ despite of the same crystalline structure for both.

To determine the origin of the observed non-zero magnetization, polarized neutron reflectometry (PNR) measurements were carried out on 1125-LSCO film (10 K and 0.9T) at the instrument multi-purpose reflectometer (MR) in China Spallation Neutron Source (CSNS) [69, 70]. PNR is a powerful tool for investigating the depth-resolved magnetization profile of thin films that is exclusively sensitive to the long-range order, and thus can eliminate the signals resulted from magnetic contamination or cluster [71]. The collected non-spin-flip specular reflectivities of polarized neutrons (R_{++} and R_{-}) for present 1125-LSCO film are shown in Fig. 8, from which the spin asymmetry (SA) as a function of wave vector transfer Q can be calculated as $SA(Q) = (R_{++} - R_{-}) / (R_{++} + R_{-})$ (see the inset of Fig. 8). The difference between R_{++} and R_{-} is rather small, and the best fit of SA yields a definite

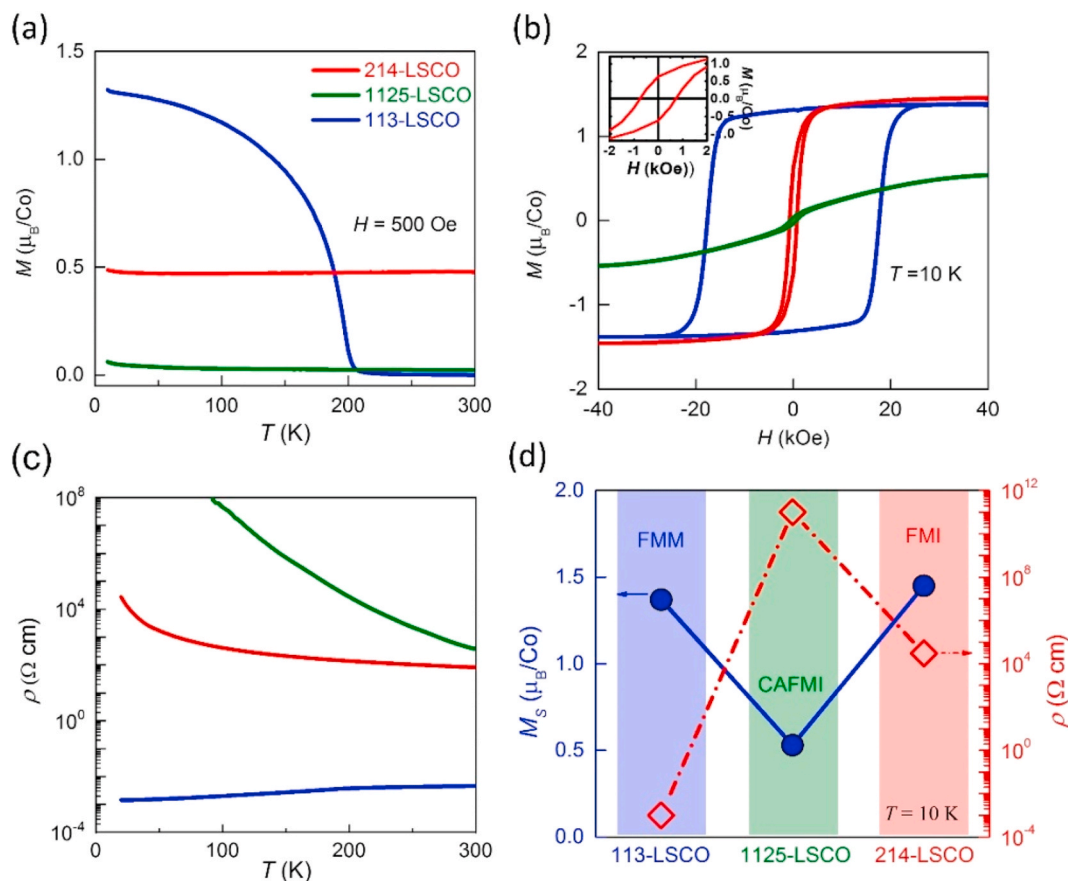


Fig. 7. Physical properties of 113-LSCO, 1125-LSCO and 214-LSCO films. (a) In-plane temperature-dependent magnetization measurements of three films measured at 500 Oe along (100) LSAT direction. (b) In-plane magnetic hysteresis loops of the three films at 10 K, where the inset shows the enlarged M-H curve of 214-LSCO film around the coercivity. (c) Temperature-dependent electrical resistivity (ρ) of the three films. (d) Evolution of magnetic and transport properties at 10 K during the tri-state topotactic transformation. FMM, ferromagnetic metal behavior; CAFMI canted-antiferromagnetic insulator behavior; FMI, ferromagnetic insulator behavior.

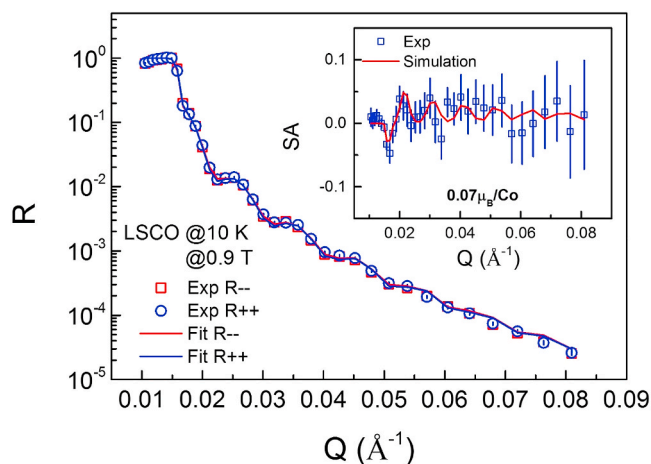


Fig. 8. PNR with the spin-dependent neutron reflectivities R_{++} and R_{-} at 10 K under a 0.9 T magnetic field applied along the in-plane direction. The inset is the Q dependence of spin asymmetry (SA).

magnetization of $0.07 \mu_B/\text{Co}$ under a magnetic field of 0.9T at 10 K (see the inset of Fig. 8). These PNR data suggest that the coherent structure of BM 1125-LSCO exhibits very weak ferromagnetism at 10 K, but the detected magnetization value is smaller than that measured from SQUID at 0.9T and 10 K ($\sim 0.23 \mu_B/\text{Co}$, see Fig. 7b). This deviation might be caused by possible oxygen vacancies and impurities in 1125-LSCO that cannot contribute to the PNR signals [71,72]. Generally, the magnetization in G-type antiferromagnetic phase is weak, and its detection is often prone to the influences of artifacts and impurities. In particular, it has been reported that valence change in Fe or Co-based oxides is accompanied by electron hopping [72], which may lead to vacancy-induced ferromagnetism that cannot be detected by PNR [69]. Nevertheless, the definite non-zero net magnetization observed in present 1125-LSCO sample may suggest that the 1125-LSCO exhibits a canted spin alignment (i.e. non-collinear antiferromagnetic magnetic structure). Such canted magnetic structure should be attributed to the distortion of CoO_6 and CoO_4 owing to the La^{3+} -doping.

With the migration of B-site Co ions upon further vacuum annealing, SQUID measurements indicate that the resulted 214-LSCO film exhibits ferromagnetic behavior in the whole measured temperature range (from 300 K to 10 K) with a saturated moment of $1.45 \mu_B/\text{Co}$ (Fig. 7b,d). Note that this magnetic behavior is contributed by both the 214-LSCO phase and the coexistent Co-clusters. To analyze the contribution from Co-clusters, inset of Fig. 7b presents the enlarged M-H curve, from which a coercivity as much as $H_c \sim 740$ Oe can be identified for the 214-LSCO film. This coercivity value is not equal to but almost 7 times larger than that ($H_c < 100$ Oe) of Co metal [73]. XPS has demonstrated the metallic nature of Co atoms in Co clusters (Fig. 4c). It can be inferred that the observed large coercivity should not come from the contribution of Co clusters, but from 214-LSCO phase. So this result indicates the ferromagnetic nature of the 214-LSCO phase. Although the precise magnetic moment for the SL 214-LSCO phase cannot be deduced directly from the present experimental results, which requires further subtle experimental investigations and may be beyond the scope of this paper, however, we can still conclude safely that the SL 214-LSCO phase obtained from the topotactic transformation has a ferromagnetic ground state, by taking into account the observed large coercivity ($H_c \sim 740$ Oe, inset of Fig. 7b) for the 214-LSCO film and the reported ferromagnetism for the $\text{La}_{1.4}\text{Sr}_{0.6}\text{CoO}_4$ bulk with the same 214-SL structure and components [74].

Moreover, the resistivity measurements show that the transport behavior of the 214-LSCO film remains insulating, but the 10 K resistivity is largely lower than that of 1125-LSCO film (Fig. 7d). Considering the embedded Co-rich clusters in the 214-LSCO film are mainly

composed of metallic elemental cobalt, one may conclude that the obtained SL 214-LSCO phase should behave insulating in the whole measured temperature range though the specific contribution from Co clusters cannot be separated from present experimental results.

3.5. The role of A-site La^{3+} -doping in the formation of Co-migration channel

It is worthy to point out that the topotactic transformation induced by the concerted migration of oxygen and Co-ions has never been realized on SrCoO_x films, either in our experiments or in previous reports. Obviously, the A-site La^{3+} -doping should play a key role in the tri-state topotactic transformation. To reveal the mechanism of such topotactic transformation facilitated by the substitution of La^{3+} for Sr^{2+} at A-site, first-principles calculations on the reaction enthalpy changes of BM-SL phase transformation were performed for both 1125-LSCO ($\text{La}_{0.7}\text{Sr}_{0.3}\text{CoO}_{2.5}$) and $\text{SrCoO}_{2.5}$ (see Supplementary Note S3). The results demonstrated that the 1125-LSCO with La^{3+} -doping at A-site shows high thermodynamic instability compared to $\text{SrCoO}_{2.5}$. The calculated reaction enthalpy change for 1125-LSCO (1.49eV) is lower than that of $\text{SrCoO}_{2.5}$ without La^{3+} doping (1.86eV), demonstrating that the La^{3+} doping at A-site reduces the thermodynamic barrier for the transformation from BM to SL phase.

These results demonstrate that the mixed valence of cobalt ions created by A-site La^{3+} -doping may play a vital role in this series of topotactic transformations (see Fig. 9a). In perovskite 113-LSCO film, the Co ions in the CoO_6 octahedron are in a mixed valence state of 70% Co^{3+} and 30% Co^{4+} . Due to the high energy of Co^{4+} valence state in multivalent cobaltites [10,12], the mixed Co^{4+} and Co^{3+} state tends to convert to more stable Co^{3+} and/or Co^{2+} state and promotes the formation of the BM structure by the oxygen ions transfer. In present BM 1125-LSCO with La^{3+} -doping, the average valence state of Co ions in the CoO_6 octahedron tends to reduce towards +3 due to the mixture of 70% La^{3+} and 30% Sr^{2+} at A-sites, resulting in an enhanced stability of the CoO_6 layer compared to that in BM $\text{SrCoO}_{2.5}$ without La^{3+} -doping (see Fig. 9b). While for CoO_4 tetrahedrons in 1125-LSCO with La^{3+} -doping, the valence state of Co ions (+2) may also tend to reduce due to the substitution of La^{3+} for Sr^{2+} considering possible charge transfer caused by covalent sharing (see details provided in Supplementary Note S4), which makes a relative weak Co-O bond in the CoO_4 tetrahedron in comparison with that in $\text{SrCoO}_{2.5}$ without La^{3+} -doping (see Fig. 9b). Moreover, theoretical calculations of cohesive energy for present 1125-LSCO further demonstrated that the Co-O bond in CoO_4 tetrahedrons is more unstable than that in the CoO_6 octahedrons (see section 3.3, Supplementary Note S3 and Note S4).

In other words, the Sr^{2+} at A-site tends to increase the content of Co^{4+} in the perovskite structure and promote the formation of the BM structure, while the La^{3+} content at A-site tends to lower the valence state of Co in the BM structure and destabilize the Co-O bond in the CoO_4 tetrahedron. Compared to SrCoO_x , the La^{3+} -doping at A-site effectively reduce the cohesive energy of the Co ions and thus the stability of the Co-O bond in CoO_4 tetrahedron of 1125-LSCO. As a result, the Co-O bond in the CoO_4 tetrahedron of 1125-LSCO breaks down and oxygen escapes from the film as the temperature increases in a process of vacuum annealing, facilitating the outflow of Co ions in the tetrahedral layer from the structural framework of BM 1125-LSCO.

3.6. Reversibility of the topotactic transformation

The reversibility is important to practical application of topotactic transformed materials, such as potential ion battery or electrocatalysis applications. By utilizing the reversed oxygen-annealing, the reversibility of the tri-state transformation from perovskite to BM and to SL was examined. It was found that the 214-phase can completely return back to the perovskite structure by annealing under oxygen atmosphere. Fig. 10 shows the comparison of XRD patterns for the sample undergoing

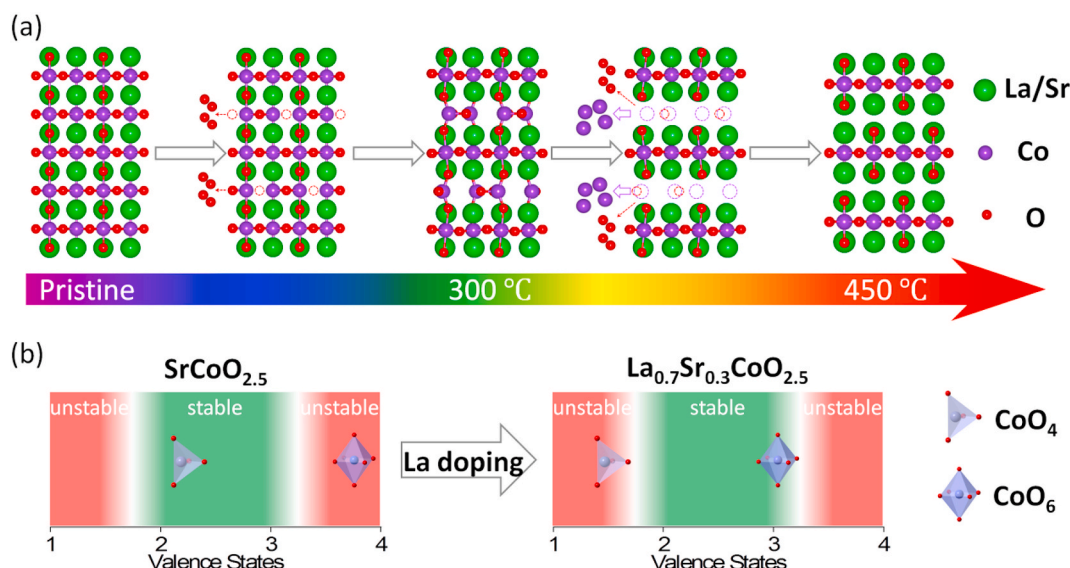


Fig. 9. Schematic diagrams of the oxygen and cobalt ions migration process. (a) Schematic diagrams of tri-phase topotactic transformations from perovskite 113-LSCO to BM 1125-LSCO to SL 214-LSCO. (b) Effects of La doping on the relative stability of CoO₄ tetrahedrons and CoO₆ octahedrons.

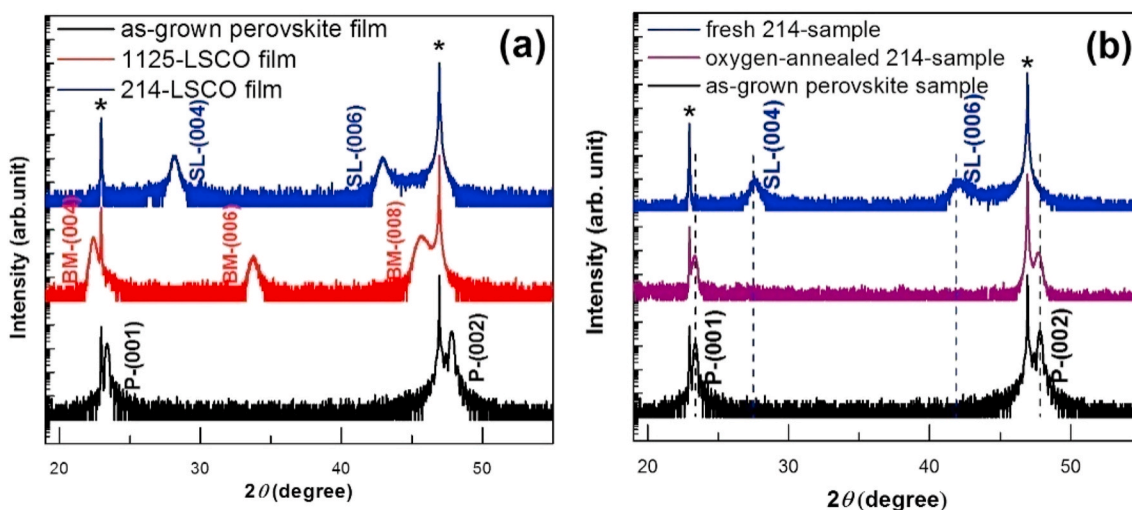


Fig. 10. (a) XRD θ - 2θ scans of the sample undergoing transformations from Perovskite to BM and to SL. (b) XRD θ - 2θ scans of 214-sample undergoing reversed transformation from SL to perovskite via annealing under flowing oxygen at 800 °C for 2hr. The diffraction peaks marked by asterisks come from substrate LSAT (001) and LSAT (002) peaks, respectively. P-(001) and P-(002) indicate perovskite characteristic peaks, BM-(004), -(006) and -(008) denote BM characteristic peaks, while SL-(004) and SL-(006) are the ones of single layered perovskite.

vacuum-annealing and reversed oxygen-annealing, respectively.

Firstly, as discussed in section 3.1, upon successive annealing at 300 °C and 450 °C under a vacuum of 10^{-6} Pa for the as-prepared 113-LSCO film, the characteristic peaks of 1125-LSCO phase (BM-(004), (006) and (008)) and 214-LSCO phase (SL-(004), (006)) emerge successively, accompanied by the disappearance of perovskite and BM characteristic peaks, respectively (see Figs. 10a and 1e), which manifests the process of tri-state transformation from perovskite to BM and to SL. While upon the oxygen-annealing for the fresh 214-LSCO film at 800 °C under flowing oxygen, perovskite characteristic peaks of P-(001) and P-(002) re-emerge at around 23.3° and 47.7°, accompanied by the disappearance of SL characteristic peaks SL-(004) and SL-(006) at about 28.9° and 42.9°, as shown in Fig. 10b. Note that there is no other phase observed in the

XRD patterns for the oxygen-annealed 214-sample, demonstrating the occurrence of a completely reversed transformation to perovskite structure. It is worth noting that there is no obvious 1125-LSCO characteristic peaks observed in the returning process for the oxygen-annealed 214-sample (Fig. 10b), which can be understandable considering the instability of 1125-LSCO under oxygen atmosphere. Actually, we found that the 1125-LSCO phase can even naturally transform to an oxygen-deficient perovskite structure when placed in air (see supplementary Fig. S10).

Moreover, the transport properties for the 214-LSCO film after oxygen-annealing have also been examined to further validate the reversibility of the presented topotactic transformation. It was found that the resistivity of 214-film significantly decreases by 5 orders of

magnitude (from $\sim 10^2 \Omega \text{ cm}$ to $\sim 10^{-3} \Omega \text{ cm}$) after the oxygen-annealing (see Supplementary Fig. S11b). Meanwhile, a metal-insulator transition reappears in the oxygen-annealed 214-film (Supplementary Fig. S11), which is similar to that in original as-grown perovskite film. The transition temperature of the oxygen-annealed 214-film, determined as 189 K from the maximum point of resistivity, is only a bit lower than that of original as-grown perovskite film (197 K) probably due to a small amount of residual oxygen defects in the oxygen-annealed 214-film. That is to say, the evolution of transport behaviors in the 214-sample upon oxygen-annealing is just the reverse of what occurs in the as-grown perovskite sample upon vacuum-annealing, where the transport behaviors transform from metal to insulation. Such opposite variation in transport behaviors further evidences that the presented topotactic transformation is completely reversible.

4. Conclusion

In summary, a tri-state topotactic transformation from perovskite to BM and to SL phase, driven by concerted transfer of oxygen and B-site Co ions, has been achieved in the $\text{La}_{0.7}\text{Sr}_{0.3}\text{CoO}_3$ film via a two-step vacuum annealing. Ac-STEM and XRD analysis demonstrated that the transfer of Co-ions is not arbitrary, but orderly along the CoO_4 tetrahedral sub-layer. XPS, XAS, EELS, PNR, magnetic and electric measurements further show that the concerted transfer of oxygen and B-site ions substantially changes the valence state, occupation of 3d orbital and spin state of Co ions, resulting in stark changes from ferromagnetic metal to canted-antiferromagnetic insulator and to ferromagnetic insulator. This unique character of modulating e_g occupancy and spin state of B-site ions in present tri-state topotactic transformation can be helpful in monitoring the dynamic change in oxygen reduction and/or evolution activities for energy generation and storage devices.

First-principles calculations revealed that the La^{3+} -doping at A-site effectively reduces the cohesive energy of Co ions in the CoO_4 tetrahedron and largely destabilize the Co–O bond in tetrahedral sub-layer of BM phase, facilitating the establishment of a distinct migration channel for Co-ions transfer in the CoO_4 tetrahedral layer. Our finding highlights the effectiveness of regulating topotactic transformation via B-site ions transfer in thin films of ABO_x complex oxides, which opens up a new approach for manipulating the reversible topotactic phase transition with diverse operational functionalities.

Declaration of competing interest

The authors declare that they have no known competing financial interests or personal relationships that could have appeared to influence the work reported in this paper.

Acknowledgements

The authors thank Prof. Q. L. Guo for his assistance in measurements of XPS. The authors acknowledge Beamline BL08U1A in Shanghai Synchrotron Radiation Facility for XAS measurements. This work was supported by the National Key Research and Development Program of China (Grant Nos. 2017YFA0303601, 2016YFA0300701, 2017YFB0702702, 2018YFA0305704, 2016YFB0700903, 2017YFA0206300, 2019YFA0704900), National Natural Sciences Foundation of China (Grant Nos. 11674378, 51971240, U1832219, 51531008, 51771223, 51590880, 11934016, 11921004), the Key Program of the Chinese Academy of Sciences, and the Strategic Priority Research Program (B) of the Chinese Academy of Sciences (Grant Nos. XDB33030200).

Appendix A. Supplementary data

Supplementary data related to this article can be found at <https://doi.org/10.1016/j.nanoen.2020.105215>.

Credit author statement

J.W., F.X.H., and B.G.S. planned and supervised the experiments. J.L. and M.X.G. contributed equally to this work. J.L. prepared the samples and carried out XRD and magnetic/transport measurements. M.X.G., M. L. and S.M. performed first-principles calculations. J.L., K.M.Q. and H.R. Z. performed the experiments of XAS, XPS and RSMs. B.H.G., P.F.N. and J.L. performed the aberration-corrected STEM, EELS and EDS measurements and analyzed the data. W.H.L., J.Z.H., H.B.Z., F.R.S., F.X.L. and C.Z. assisted the measurements of magnetic and transport properties. T.Z. performed the PNR measurements and analyzed the data. J.W., F.X.H., J.L. and B.G.S. prepared the manuscript and refined the paper. T. W., J.D.G. and J.R.S. made scientific comments on the manuscript. All authors discussed the results and contributed to the refinement of the paper. All authors have given approval to the final version of the manuscript.

References

- [1] C. Song, B. Cui, F. Li, X. Zhou, F. Pan, Prog. Mater. Sci. 87 (2017) 33–82.
- [2] Z. Zhang, D. Schwanz, B. Narayanan, M. Kotiuga, J.A. Dura, M. Cherukara, H. Zhou, J.W. Freeland, J. Li, R. Sarturo, F. He, C. Wu, J. Zhu, Y. Sun, K. Ramadoss, S.S. Nonnenmann, N. Yu, R. Comin, K.M. Rabe, S.K.R.S. Sankaranarayanan, S. Ramanathan, Nature 553 (2017) 68.
- [3] Y. Zhou, X. Guan, H. Zhou, K. Ramadoss, S. Adam, H. Liu, S. Lee, J. Shi, M. Tsuchiya, D.D. Fong, S. Ramanathan, Nature 534 (2016) 231–234.
- [4] J. Maier, Nat. Mater. 4 (2005) 805.
- [5] D.V. Christensen, Y. Frenkel, Y.Z. Chen, Y.W. Xie, Z.Y. Chen, Y. Hikita, A. Smith, L. Klein, H.Y. Hwang, N. Pryds, B. Kalisky, Nat. Phys. 15 (2019) 269–274.
- [6] X.R. Wang, C.J. Li, W.M. Lü, T.R. Paudel, D.P. Leusink, M. Hoek, N. Poccia, A. Vailionis, T. Venkatesan, J.M.D. Coey, E.Y. Tsymlab, Ariando, H. Hilgenkamp, Science 349 (2015) 716.
- [7] Z.Q. Liu, C.J. Li, W.M. Lü, X.H. Huang, Z. Huang, S.W. Zeng, X.P. Qiu, L.S. Huang, A. Annadi, J.S. Chen, J.M.D. Coey, T. Venkatesan, Ariando, Phys. Rev. X 3 (2013), 021010.
- [8] H. Zhang, Y. Yun, X. Zhang, H. Zhang, Y. Ma, X. Yan, F. Wang, G. Li, R. Li, T. Khan, Y. Chen, W. Liu, F. Hu, B. Liu, B. Shen, W. Han, J. Sun, Phys. Rev. Lett. 121 (2018) 116803.
- [9] Y.Z. Chen, N. Bovet, F. Trier, D.V. Christensen, F.M. Qu, N.H. Andersen, T. Kasama, W. Zhang, R. Giraud, J. Dufouleur, T.S. Jespersen, J.R. Sun, A. Smith, J. Nygård, L. Lu, B. Büchner, B.G. Shen, S. Linderoth, N. Pryds, Nat. Commun. 4 (2013) 1371.
- [10] N. Lu, P. Zhang, Q. Zhang, R. Qiao, Q. He, H.B. Li, Y. Wang, J. Guo, D. Zhang, Z. Duan, Z. Li, M. Wang, S. Yang, M. Yan, E. Arenholz, S. Zhou, W. Yang, L. Gu, C. W. Nan, J. Wu, Y. Tokura, P. Yu, Nature 546 (2017) 124–128.
- [11] Y. Tsujimoto, C. Tassel, N. Hayashi, T. Watanabe, H. Kageyama, K. Yoshimura, M. Takano, M. Ceretti, C. Ritter, W. Paulus, Nature 450 (2007) 1062–1065.
- [12] H. Jeon, W.S. Choi, M.D. Biegalski, C.M. Folkman, I.C. Tung, D.D. Fong, J. W. Freeland, D. Shin, H. Ohta, M.F. Chisholm, H.N. Lee, Nat. Mater. 12 (2013) 1057–1063.
- [13] Y.-M. Kim, A. Morozovska, E. Eliseev, M.P. Oxley, R. Mishra, S.M. Selbach, T. Grande, S.T. Pantelides, S.V. Kalinin, A.Y. Borisevich, Nat. Mater. 13 (2014) 1019.
- [14] Z.Q. Liu, D.P. Leusink, X. Wang, W.M. Lü, K. Gopinadhan, A. Annadi, Y.L. Zhao, X. H. Huang, S.W. Zeng, Z. Huang, A. Srivastava, S. Dhar, T. Venkatesan, Ariando, Phys. Rev. Lett. 107 (2011) 146802.
- [15] Z. Shao, S.M. Haile, Nature 431 (2004) 170.
- [16] M.A. Peña, J.L.G. Fierro, Chem. Rev. 101 (2001) 1981–2018.
- [17] J.K. Nørskov, T. Bligaard, J. Rossmeisl, C.H. Christensen, Nat. Chem. 1 (2009) 37–46.
- [18] H.B. Li, N. Lu, Q. Zhang, Y. Wang, D. Feng, T. Chen, S. Yang, Z. Duan, Z. Li, Y. Shi, W. Wang, W.H. Wang, K. Jin, H. Liu, J. Ma, L. Gu, C. Nan, P. Yu, Nat. Commun. 8 (2017) 2156.
- [19] Y. Sun, M. Kotiuga, D. Lim, B. Narayanan, M. Cherukara, Z. Zhang, Y. Dong, R. Kou, C.-J. Sun, Q. Lu, I. Waluyo, A. Hunt, H. Tanaka, A.N. Hattori, S. Gamage, Y. Abate, V.G. Pol, H. Zhou, S.K.R.S. Sankaranarayanan, B. Yildiz, K.M. Rabe, S. Ramanathan, Proc. Natl. Acad. Sci. U.S.A. 115 (2018) 9672.
- [20] S.W. Zeng, X.M. Yin, T.S. Herg, K. Han, Z. Huang, L.C. Zhang, C.J. Li, W.X. Zhou, D.Y. Wan, P. Yang, J. Ding, A.T.S. Wee, J.M.D. Coey, T. Venkatesan, A. Rusydi, A. Ariando, Phys. Rev. Lett. 121 (2018) 146802.
- [21] R. Waser, R. Dittmann, G. Staikov, K. Szot, Adv. Mater. 21 (2009) 2632–2663.
- [22] X. Liu, L. Zhang, Y. Zheng, Z. Guo, Y. Zhu, H. Chen, F. Li, P. Liu, B. Yu, X. Wang, J. Liu, Y. Chen, M. Liu, Adv. Sci. 6 (2019) 1801898.
- [23] J.Z. Chen, H.B. Tao, B. Liu, Adv. Energy Mater. 7 (2017) 1700886.
- [24] Y. Ding, I.S. Yang, Z.Q. Li, X. Xia, W.I. Lee, S.Y. Dai, D.W. Bahnemann, J.H. Pan, Prog. Mater. Sci. 109 (2020) 100620.
- [25] M. Wang, S. Shen, J. Ni, N. Lu, Z. Li, H.B. Li, S. Yang, T. Chen, J. Guo, Y. Wang, H. Xiang, P. Yu, Adv. Mater. 29 (2017) 1703628.
- [26] Y. Cui, G. Zhang, H. Li, H. Lin, X. Zhu, H.-H. Wen, G. Wang, J. Sun, M. Ma, Y. Li, D. Gong, T. Xie, Y. Gu, S. Li, H. Luo, P. Yu, W. Yu, Sci. Bull. 63 (2018) 11–16.
- [27] A.G. Dustin, J.G. Alexander, Nat. Mater. 18 (2019) 2–3.

- [28] C. Leighton, *Nat. Mater.* 18 (2019) 13–18.
- [29] B. Cui, C. Song, F. Li, X.Y. Zhong, Z.C. Wang, P. Werner, Y.D. Gu, H.Q. Wu, M. S. Saleem, S.S.P. Parkin, F. Pan, *Phys. Rev. Appl.* 8 (2017), 044007.
- [30] R. Le Toquin, W. Paulus, A. Cousson, C. Prestipino, C. Lamberti, *J. Am. Chem. Soc.* 128 (2006) 13161–13174.
- [31] J. Zhang, Z. Zhong, X. Guan, X. Shen, J. Zhang, F. Han, H. Zhang, H. Zhang, X. Yan, Q. Zhang, L. Gu, F. Hu, R. Yu, B. Shen, J. Sun, *Nat. Commun.* 9 (2018) 1923.
- [32] M. Armand, J.M. Tarascon, *Nature* 451 (2008) 652.
- [33] J.M. Tarascon, M. Armand, *Nature* 414 (2001) 359.
- [34] M.D. Slater, D. Kim, E. Lee, C.S. Johnson, *Adv. Funct. Mater.* 23 (2013) 947–958.
- [35] D. Kong, M. Zhang, Y. Xiao, J. Hu, W. Zhao, L. Han, F. Pan, *Nano Energy* 59 (2019) 327–335.
- [36] F. Xiong, S. Tan, Q. Wei, G. Zhang, J. Sheng, Q. An, L. Mai, *Nano Energy* 32 (2017) 347–352.
- [37] J. Suntivich, H.A. Gasteiger, N. Yabuuchi, H. Nakanishi, J.B. Goodenough, Y. Shao-Horn, *Nat. Chem.* 3 (2011) 546–550.
- [38] J. Suntivich, K.J. May, J.B. Goodenough, H.A. Gasteiger, Y. Shao-Horn, *Science* 334 (2011) 1383–1385.
- [39] Wesley T. Hong, Marcel Risch, Kelsey A. Stoerzinger, Alexis Grimaud, Suntivich Jin, Yang Shao-Horn, *Energy Environ. Sci.* 8 (2015) 1404.
- [40] M.A. Senaris-Rodriguez, J.B. Goodenough, *J. Solid State Chem.* 118 (1995) 323–336.
- [41] R. Larsson, L.Y. Johansson, *J. Power Sources* 32 (1990) 253–260, 35.
- [42] J.T. Mefford, X. Rong, A.M. Abakumov, W.G. Hardin, S. Dai, A.M. Kolpak, K. P. Johnston, K.J. Stevenson, *Nat. Commun.* 7 (2016) 11053.
- [43] J. Walter, S. Bose, M. Cabero, G. Yu, M. Greven, M. Varela, C. Leighton, *Phys. Rev. Mater.* 2 (2018) 111404.
- [44] M. Björck, G.GenX. Andersson, *J. Appl. Crystallogr.* 40 (2007) 1174–1178.
- [45] Z. Cai, Y. Kuru, J.W. Han, Y. Chen, B. Yildiz, *J. Am. Chem. Soc.* 133 (2011) 17696–17704.
- [46] A.D. Rata, A. Herklotz, K. Nenkov, L. Schultz, K. Dorr, *Phys. Rev. Lett.* 100 (2008), 076401.
- [47] S. Inoue, M. Kawai, N. Ichikawa, H. Kageyama, W. Paulus, Y. Shimakawa, *Nat. Chem.* 2 (2010) 213–217.
- [48] S.N. Rudlesden, P. Popper, *Acta Crystallogr.* 10 (1957) 538–539.
- [49] E.J. Crumlin, E. Mutoro, S.-J. Ahn, G.J. Ia O', D.N. Leonard, A. Borisevich, M. D. Biegalski, H.M. Christen, Y. Shao-Horn, *J. Phys. Chem. Lett.* 1 (2010) 3149–3155.
- [50] J.R. Petrie, C. Mitra, H. Jeen, W.S. Choi, T.L. Meyer, F.A. Reboredo, J.W. Freeland, G. Eres, H.N. Lee, *Adv. Funct. Mater.* 26 (2016) 1564–1570.
- [51] R.F. Klie, J.C. Zheng, Y. Zhu, M. Varela, J. Wu, C. Leighton, *Phys. Rev. Lett.* 99 (2007), 047203.
- [52] L. Karvonen, M. Valkeapää, R.-S. Liu, J.-M. Chen, H. Yamauchi, M. Karppinen, *Chem. Mater.* 22 (2010) 70–76.
- [53] R.U. Chandrasena, W. Yang, Q. Lei, M.U. Delgado-Jaime, K.D. Wijesekara, M. Gollalikhani, B.A. Davidson, E. Arenholz, K. Kobayashi, M. Kobata, F.M. de Groot, U. Aschauer, N.A. Spaldin, X. Xi, A.X. Gray, *Nano Lett.* 17 (2017) 794–799.
- [54] X.Y. Wang, K.K. Huang, W. Ma, Y.G. Cong, C.D. Ge, S.H. Feng, *Chem. Eur J.* 22 (2016) 1–9.
- [55] L. Dahéron, R. Dedryvère, H. Martinez, M. Ménétrier, C. Denage, C. Delmas, D. Gonbeau, *Chem. Mater.* 20 (2008) 583–590.
- [56] J. Yang, H. Liu, W.N. Martens, R.L. Frost, *J. Phys. Chem. C* 114 (2010) 111–119.
- [57] M.C. Biesinger, B.P. Payne, A.P. Grosvenor, L.W.M. Lau, A.R. Gerson, R.S.C. Smart, *Appl. Surf. Sci.* 257 (2011) 2717–2730.
- [58] A.S. Walton, J. Fester, M. Bajdich, M.A. Arman, J. Osiecki, J. Knudsen, A. Vojvodic, J.V. Lauritsen, *ACS Nano* 9 (2015) 2445–2453.
- [59] S.C. Petitto, E.M. Marsh, G.A. Carson, M.A. Langell, *J. Mol. Catal. Chem.* 281 (2008) 49–58.
- [60] J. Yu, G. Chen, J. Sunarso, Y. Zhu, R. Ran, Z. Zhu, W. Zhou, Z. Shao, *Adv. Sci.* 3 (2016) 1600060.
- [61] Y. Zhu, H. Bai, Y. Huang, *J. Phys. Condens. Matter* 28 (2016), 045303.
- [62] Y. Ding, Y. Wang, *Nanoscale Res. Lett.* 10 (2015) 13.
- [63] M. Hayward, E. Cussen, J. Claridge, M. Bieringer, M. Rosseinsky, C. Kiely, S. Blundell, I. Marshall, F. Pratt, *Science* 295 (2002) 1882–1884.
- [64] S. Hu, Y. Wang, C. Cazorla, J. Seidel, *Chem. Mater.* 29 (2017) 708–717.
- [65] J.H. Jang, Y.-M. Kim, Q. He, R. Mishra, L. Qiao, M.D. Biegalski, A.R. Lupini, S. T. Pantelides, S.J. Pennycook, S.V. Kalinin, *ACS Nano* 11 (2017) 6942–6949.
- [66] Q. Lu, B. Yildiz, *Nano Lett.* 16 (2016) 1186–1193.
- [67] D. Fuchs, M. Merz, P. Nagel, R. Schneider, S. Schuppler, H. von Lohneysen, *Phys. Rev. Lett.* 111 (2013) 257203.
- [68] A. Muñoz, C. de la Calle, J.A. Alonso, P.M. Botta, V. Pardo, D. Baldomir, J. Rivas, *Phys. Rev. B* 78 (2008), 054404.
- [69] C. Liu, F. An, Paria S.M. Gharavi, et al., *Natl. Sci. Rev.* 7 (2020) 84.
- [70] H. Bai, X.Z. Zhan, Gang Li, Jian Su, Z.Z. Zhu, Ying Zhang, T. Zhu, J.W. Cai, *Appl. Phys. Lett.* 115 (2019) 182401.
- [71] X. Zhai, A.J. Grutter, Y. Yu, Z. Cui, Y. Lu, *Phys. Rev. Mater.* 2 (2018), 044405.
- [72] J.M.D. Coey, A.P. Douvalis, C.B. Fitzgerald, M. Venkatesan, *Appl. Phys. Lett.* 84 (2004) 1332.
- [73] J. Camarero, J.J. de Miguel, R. Miranda, A. Hernando, *J. Phys. Condens. Matter* 12 (2000) 7713.
- [74] Y. Furukawa, S. Wada, Y. Yamada, *J. Phys. Soc. Jpn.* 62 (1993) 1127.



Jia Li received Ph.D. degree from the Institute of Physics, Chinese Academy of Sciences under the supervision of Prof. Feng-xia Hu in 2020. His research interests are spin order regulation under multiple fields and novel physical property of complex oxide films.



Meng-xue Guan received Ph.D degree from Institute of Physics, Chinese Academy of Science under the supervision of Professor Sheng Meng in 2020. Her current research interests focus on first-principle simulations of fundamental electronic properties and ultrafast dynamics in condensed-matter systems.



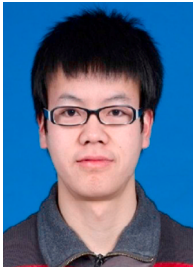
Peng-fei Nan is currently a Ph.D. candidate under Prof. Binghui Ge in the Institute of Physics, Chinese Academy of Sciences and the Institutes of Physical Science and Information Technology of Anhui University, mainly engaged in the electron microscopy characterization of functional and environmentally friendly materials including perovskite oxides.



Jing Wang is currently an associate professor in Institute of Physics, Chinese Academy of Science. He received his Ph.D. degree at Institute of Physics, Chinese Academy of Science in 2001. His current research interests focus on the regulation effect of topotactic transformation, interface carrier doping, interlayer coupling, strain and ion-defects in strongly correlated electron systems, and various caloric effects relating to order-disorder phase transitions.



Prof. Bing-hui Ge is currently the director of the Electron Microscope Center of Anhui University. He mainly focuses on the research of aberration corrected electron microscopy, image contrast theory and electronic crystallography, as well as in-situ electron microscopy characterization of functional and environmentally friendly materials including complex oxides.



Kai-ming Qiao is currently a Ph.D. candidate under the supervision of Prof. Fengxia Hu at Institute of Physics, Chinese Academy of Sciences. His research interests focus on multi-field modulated magnetocaloric effect in first order phase transition materials and the field-regulated interface spin state in complex oxides.



Fei-xiang Liang received his Ph.D. degree on Condensed Matter of Physics in 2019 at Institute of Physics, Chinese Academy of Sciences. His current research focuses on oxide materials exhibiting functional properties associated with structural transitions, with a special attention paid to the interplay between different ferroic properties.



Hong-rui Zhang received Ph.D. degree from Institute of Physics, Chinese Academy of Science in 2019. His research is focusing on the regulated magnetism under multiple fields and spin-polarized two-dimensional electron gases at oxide interface.



Hou-bo Zhou is pursuing Ph.D. degree currently in the Institute of Physics, Chinese Academy of Sciences under the supervision of Prof. Feng-xia Hu. The main direction of his research is the oxide interfacial state and interface spin regulation.



Wen-hui Liang received Ph.D. degree from Institute of Physics, Chinese Academy of Sciences under the supervision of Prof. Feng-Xia Hu in 2020. Her research interests include the multiferroics and regulated magnetism under multiple fields in thin films of strongly correlated electron systems.



Cheng Zhang is currently a Ph.D. candidate in the Institute of Physics, Chinese Academy of Sciences, mainly focuses on the interface quantum state control of strongly correlated electronic system.



Jia-zheng Hao received Ph.D. degree under the supervision of Prof. Feng-xia Hu at the Institute of Physics, Chinese Academy of Sciences in 2020. Her scientific interest is focusing on magnetism and magnetic materials with an emphasis on structure, multicaloric effects, oxide spintronics and interface orbital reconstruction of materials.



Miao Liu, as an associate professor of the Institute of Physics, Chinese Academy of Science, works on the field of data-driven materials science, which includes high-throughput DFT, strongly correlated materials design, and AI-aided materials discovery.



Fei-ran Shen is pursuing his Ph.D. degree under the supervision of Prof. Feng-xia Hu at the Institute of Physics, Chinese Academy of Sciences. His research interests focus on magnetic ordering dominated baromagnetic effect in various materials by using neutron scattering.



Sheng Meng is a professor of Institute of Physics, Chinese Academy of Science since 2009. His research interests are centered on excited state electron dynamics in condensed matters and energy conversion mechanism for sustainable society.



Tao Zhu is a Professor at Institute of Physics, Chinese Academy of Science since 2007. He received his Ph.D. degree in Materials from Zhejiang University in 1997. In the past ten years, he designed and fabricated neutron reflectometer at China spallation neutron source. His current research interests focus on the novel magnetic properties in thin films by using polarized neutron reflectometry.



Jian-dong Guo received his Ph.D. degree in condensed matter physics from the Institute of Physics, Chinese Academy of Sciences, in 2001. Then he worked in University of Tennessee, US, as a postdoctoral research associate. In 2005, he returned to China and joined the Institute of Physics as a professor. His research interests include the design and growth of low-dimensional oxide structure, as well as the collective excitations of the surfaces & interfaces of complex materials.



Feng-xia Hu is a Professor at Institute of Physics, Chinese Academy of Science since 2008. She received her Ph.D. degree at Institute of Physics, Chinese Academy of Science in 2002 with major of condensed matter physics. Her current interests include magnetocaloric effect and its regulation by multifold, oxide spintronics and interface orbital reconstruction and spin regulation.



Ji-rong Sun is a Professor of Condensed Matter Physics in Institute of Physics of the Chinese Academy of Sciences since 1999. He received his Ph.D. degree at Institute of Physics, Chinese Academy of Sciences in 1989. His current research interests focus on transport behavior of spin polarized electrons in oxides and fabrication, characterization of the hetero-epitaxial multilayers of various perovskite oxides, and the effects of size, interface, intra- and interlayer coupling.



Tom Wu received his B.S. degree from Zhejiang University in 1995 and Ph.D. degree from the University of Maryland, College Park in 2002. Before joining University of New South Wales (UNSW) in Sydney as a full professor, he worked as postdoc in Argonne National Laboratory in Chicago, assistant professor in Nanyang Technological University (NTU) Singapore, and associate professor in King Abdullah University of Science and Technology (KAUST). Dr. Wu works in the areas of oxide thin films, nanomaterials, and hybrid perovskites, with a focus on their electronic, magnetic and optical functionalities.



Bao-gen Shen is a Professor at Institute of Physics, Chinese Academy of Science since 1995. His current research interests focus on magnetic properties and magnetocaloric effects of rare-earth-transition-metal compounds, topological magnetism, spintronics of various complex oxides.